Optically Driven Dynamics of a Mott Insulator-to-Metal Transition

Ksenia S. Rabinovich, Alexander N. Yaresko, Robert D. Dawson, Maximilian J. Krautloher, Tim Priessnitz, Yves-Laurent Mathis, Andrei Kirilyuk, Bernhard Keimer, and Alexander V. Boris*

Fundamental understanding and on-demand control of correlation-driven insulator-to-metal transitions (IMTs) via nonequilibrium drive are prime targets of current materials research, especially in view of a host of potential applications in a wide range of next-generation quantum devices. Photoinduced switching between competing orders in correlated insulators requires a free-energy landscape with nearly degenerate ground states, which is commonly reached in 3d-electron materials through heavy doping, strain, or the application of static electric fields. The associated spatial inhomogeneity leads to a photoinduced phase transition (PIPT) that remains confined near the illuminated region. Here, optical spectroscopy experiments are reported within the hysteretic region at the first-order IMT in the 4d-electron compound $Ca_3(Ru_{0.99}Ti_{0.01})_2O_7$ and show that specific Ru $t_{2g}d_\uparrow \rightarrow d_\downarrow$ interband transitions resonantly excited by light with a threshold fluence corresponding to the planar density of Ru atoms can trigger reversible, avalanche-like coherent propagation of phase interfaces across the full extent of a macroscopic sample, in the absence of assisting external stimuli. Based on detailed comparison of spectroscopic data to density functional calculations, we attribute the extraordinary photo-sensitivity of the IMT to an exceptionally shallow free-energy landscape generated by the confluence of electron–electron and electron-lattice interactions. These findings highlight $Ca_3(Ru_{0.99}Ti_{0.01})_2O_7$ as a powerful model system for building and testing a theory of Mott transition dynamics in the presence of strong electron-lattice coupling and may pave the way toward nanoscale devices with quantum-level photosensitivity.

1. Introduction

Light control over phase transitions in perovskite transition metal oxides requires precise tuning of the intrinsic collective instabilities involving spin, charge, orbital, and lattice degrees of freedom.[1–4] Rotations and distortions of the octahedral network give rise to a delicate interplay between the underlying electronic, magnetic, and crystal structure. Competition between these different degrees of freedom has been extensively studied by ultrafast pump-probe spectroscopy, which has revealed short-lived, transient electronic and magnetic states that are not thermally accessible in equilibrium.[5,6] The colossal magnetoresistive manganites have been observed to exhibit long-lived and reversible light-induced phase switching between antiferromagnetic (AFM) charge-ordered insulating and ferromagnetic (FM) metallic states.[3,4,7,8] However, this transition from localized spin to itinerant electron behavior requires an assisting external stimulus, such as a static electric field or epitaxial strain, and remains spatially confined to the illuminated region. Magnetoelastic effects are essential to stabilize

K. S. Rabinovich, A. N. Yaresko, R. D. Dawson, M. J. Krautloher,
T. Priessnitz, B. Keimer, A. V. Boris
Max Planck Institute for Solid State Research
Heisenbergstraße 1, 70569 Stuttgart, Germany
E-mail: A.Boris@fkf.mpg.de

Y.-L. Mathis
Institute for Beam Physics and Technology
Karlsruhe Institute of Technology
76344 Eggenstein - Leopoldshafen, Germany
A. Kirilyuk
HFML-FELIX Laboratory
Radboud University
Toernooiveld 7, Nijmegen 6525 ED, Netherlands

AFM insulating and FM metallic phases in a nearly degenerate configuration.

The high level of stability of the charge-ordered insulating phase in manganites is a consequence of the strong tendency of its $3d$ valence electrons to localize as a result of the high ratio of Coulomb interaction to bandwidth. This propensity for electrons to localize is reduced in $4d$-electron materials, particularly ruthenates. This compound family thus offers an auspicious path toward achieving robust light-sensitive phase control, owing to the delicate balance between the competing energy scales of collective instabilities, electronic correlations, and enhanced spin-orbit coupling. Since $4d$ orbitals are more extended, electron correlations are reduced and the ligand field strength is increased. Due to the large crystal field splitting, the Ru^{4+} ions host a low-spin $S = 1$ state with four electrons in the t_{2g} manifold, such that the spin-orbit interaction enters as an important energy scale together with Coulomb repulsion and Hunds coupling. The resulting shallow energy landscape leads to a diverse array of exotic ground states where small light-induced perturbations are expected to cause switching between different phases.

Such extreme sensitivity drives ruthenates, in particular, to exhibit a high degree of susceptibility to isovalent substitution of Ru ions. Here, we focus on the $Ca_3Ru_2O_7$ bilayer perovskite system whose ground state is a polar metal,[9–15] in contrast to its Mott insulating single-layer counterpart Ca_2RuO_4.[16–18] Even a minimal substitution of Ru with just 1% Ti in $Ca_3(Ru_{1-x}Ti_x)_2O_7$ reverts the system to its insulating ground state.[19–21] At room temperature the structural, magnetic, and electronic transport properties of $Ca_3(Ru_{0.99}Ti_{0.01})_2O_7$ closely resemble those of pristine $Ca_3Ru_2O_7$. Both compounds are paramagnetic metals (PM-M) and adopt an orthorhombic crystal structure with polar space group $Bb2_1m$. However, upon cooling the two compounds exhibit remarkably distinct behaviors. $Ca_3Ru_2O_7$ experiences a pair of consecutive transitions in which AFM-a magnetic ordering at $T_N = 56$ K (FM (AFM) within (between) bilayers) is followed by a metamagnetic spin reorientation transition into the AFM-b phase that occurs concomitantly with an isostructural transition ($T_s = 48$ K), with weak changes in lattice parameters of less than 0.1% within.[12,15,22] Despite the pseudogap opening due to Fermi surface reconstruction at T_s, the material remains a polar metal, with itinerant electrons persisting within the ferromagnetically ordered bilayers.[10,11,14] In marked contrast to the pristine compound, $Ca_3(Ru_{0.99}Ti_{0.01})_2O_7$ exhibits a single isostructural IMT transition at $T_{IMT} = 55$ K from itinerant to localized electronic behavior with the Ru magnetic moments aligned antiferromagnetically (G-AFM-I) within the bilayers, which is associated with significant disproportionate changes in the crystal lattice parameters $\Delta b/b = 1.23\%$ and $\Delta c/c = -0.97\%$, and a minute change in a, $\Delta a/a = 0.05\%$.[21]

2. Results and Discussion
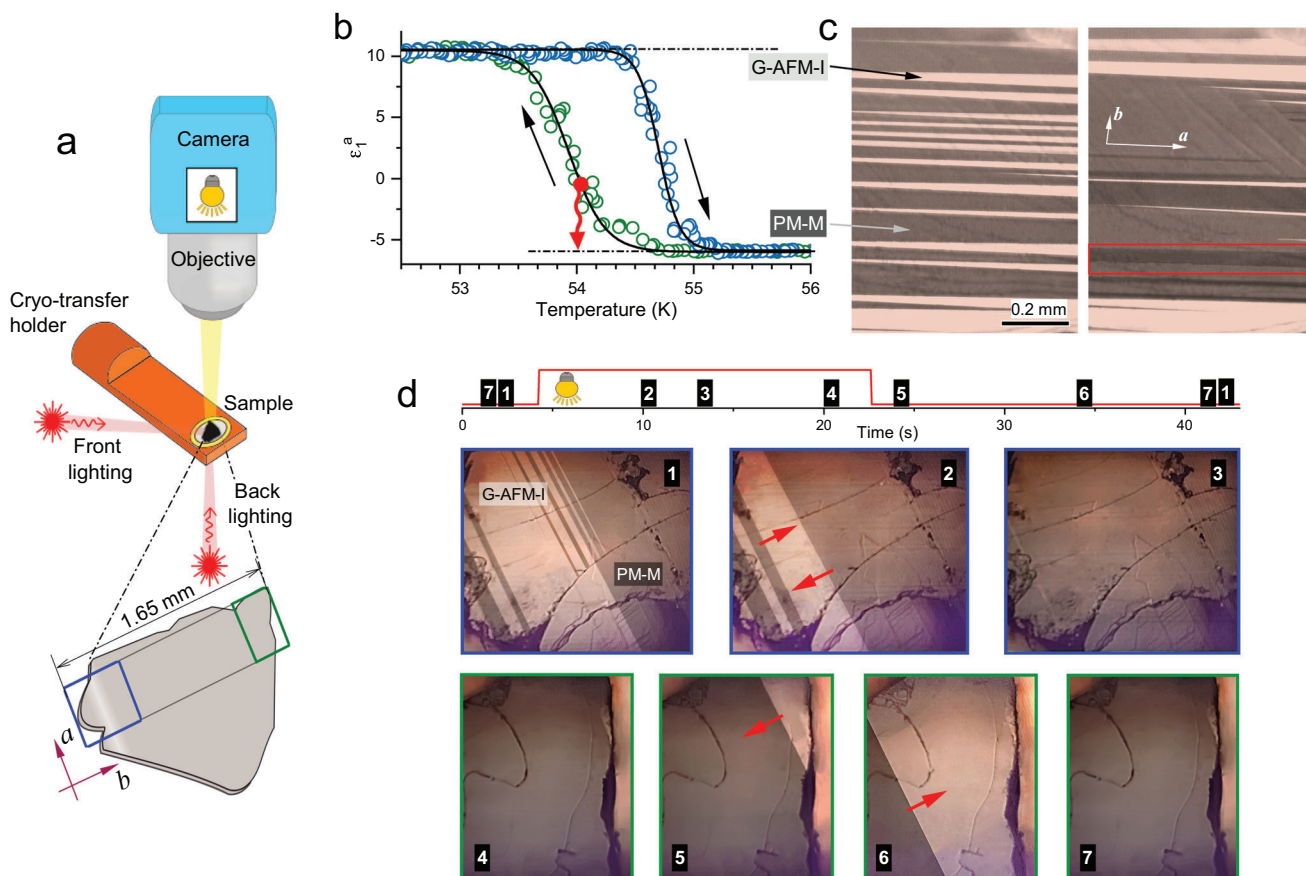
2.1. Photoinduced Insulator-to-Metal Switching

The central issue of this report is our observation of photoinduced phase switching in the near-threshold behavior of $Ca_3(Ru_{0.99}Ti_{0.01})_2O_7$. The temperature driven phase transition at T_{IMT} is first-order and characterized by hysteresis and phase separation. Within the hysteresis loop, both phases coexist as stripes,

revealing the significant influence of elastic strain resulting from disproportionate changes in the crystal lattice parameters. The concomitant spontaneous elastic strain is adapted by the formation of interfacial domain walls along the a axis, extending obliquely deep into the bulk of the sample.[23] We use conventional far-field spectroscopy to monitor the hysteretic behavior near the transition point by combining reflected light microscopy (**Figure 1**a) with scanning the dielectric permittivity ϵ_1 at $\hbar\omega = 0.6$ eV during cooling and heating cycles of the sample (Figure 1a). Notably, the hysteresis loop remains nearly symmetrical, and the domain dynamics are smooth, with no apparent domain pinning, undisturbed by the minimal isovalent substitution. We find a direct correspondence between the contrast of stripe domains (Figure 1c) and the in-plane permittivity values of the G-AFM-I ($\epsilon_1 \approx 10$) and PM-M ($\epsilon_1 \approx -6$) phases coexisting within the hysteresis loop. Whereas only the G-AFM-I and PM-M phases stabilize at slow cooling ($\lesssim 3$ K min^{-1}) where thermodynamic equilibrium is maintained, additional dark contrast is detected when the temperature is cycled at a fast cooling rate ($\simeq 5.2$ K min^{-1}). We suggest that the regions of strong dark contrast represent possible transient trapping of a metastable FM bilayer metallic phase (AFM-a or b), consistent with the near-degeneracy of the two types of magnetic order discussed below. The static stripe pattern is stabilized by the temperature at any point within the hysteresis loop, and by applying low fluence light, the sample displays a complete switch into the dark contrast PM-M state.

To clearly visualize the photoinduced switching behavior, we stabilize the stripe pattern present in frame 1 of Figure 1d at ∼54 K while cooling under low background illumination, which corresponds to the red point in Figure 1b. When white light illumination is increased above a threshold intensity of only ∼1 mW cm^{-2}, the existing dark PM-M stripes rapidly expand to cover the entire sample with a characteristic stripe domain wall velocity of 0.3 mm s^{-1}. The resulting steady-state non-equilibrium metallic state persists over the entire volume of the sample as long as the light illumination remains above the threshold irradiance. When the light intensity is reduced to the background level, the recovery of the exact initial stripe domain morphology occurs over ten seconds and begins with spontaneous nucleation of the G-AFM-I domain at the opposite end of the sample, which exhibits re-entrant behavior. To effectively capture a complete view of the photoinduced switching process we provide real-time recorded Video S3 in the Supporting Information.[24]

The stripe domain structure, featuring interfacial domain walls extending obliquely deep into the bulk of the sample, and its light-induced evolution underscore the transition's bulk nature. When the illumination intensity exceeds the threshold, we find an avalanche-like enlargement of the metal domains with the successive conversion of the insulating domains due to the essentially coherent motion of the domain walls throughout the entire crystal volume. Experimental data obtained in the back lighting geometry directly corroborate the bulk nature of the transition (see the Supporting Information[24]). This stands in stark contrast to the behavior observed in manganites, where the PIPT remains confined near the illuminated region.[3,4,7]

In the following, we develop an assessment of the intrinsic instabilities in the electronic, magnetic, and structural properties of $Ca_3(Ru_{0.99}Ti_{0.01})_2O_7$ to place the light switching behavior into full context. We discuss these instabilities and their manifestations
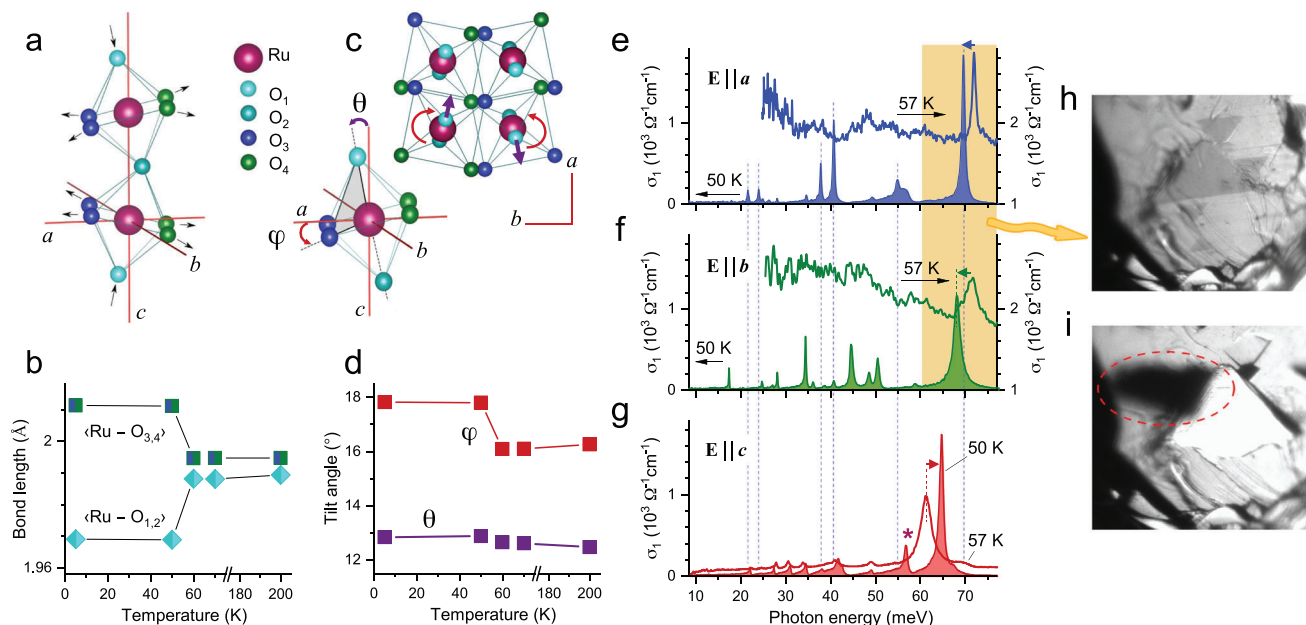
Figure 1. Stripe phase and photoinduced Mott insulator-to-metal transition in $Ca_3(Ru_{0.99}Ti_{0.01})_2O_7$. a) Schematic of the reflected light microscopy setup, equipped with a tungsten-halogen white-light lamp. In addition, the sample is illuminated from either the front side or back side. b) Dielectric permittivity measured at photon energy $\hbar\omega = 0.6$ eV upon cooling (green points) and warming (blue points). The hysteresis curve represents switching between the antiferromagnetic insulating G-AFM-I and paramagnetic metallic PM-M phases with positive and negative permittivity values, respectively. Both phases coexist as stripes inside the hysteresis loop. c) Snapshots of stripe formation from Videos S1 and S2 in the Supporting Information[24] recorded during slow cooling ($\lesssim$ 3 K min^{-1}, left panel) and fast cooling ($\simeq$5.2 K/min, right panel). Bright regions correspond to the G-AFM-I phase and dark regions to the PM-M phase. During fast cooling, additional metastable stripes are detected, as evident from regions of stronger dark contrast, highlighted by the red box. d) Illustration of the reversible photoinduced switching between G-AFM-I and PM-M phases with front side white light illumination. The numbers and corresponding frames represent different moments along the timeline of the recorded Video S3 in the Supporting Information,[24] and at different locations on the sample (frames 1 to 3 located at the blue box and frames 4 to 7 at the green box in (a). In frame 1, captured under background light with intensity of ~0.2 mW cm^{-2}, the coexisting phases are stabilized by temperature at the red dot in (b). Following the increase of microscope light irradiance reaching the sample surface to above the threshold of ~1 mW/cm^2, the PM-M phase rapidly expands over the full macroscopic extent of the sample (frames 2 to 4) and the entire crystal enters the supercooled metallic phase indicated by the end of the red arrow in (b). When the white light intensity is reduced to the background intensity before time 5, the insulating G-AFM-I phase spontaneously reappears at the opposite end of the sample and then the original phase configuration of the sample is restored (frames 7 and 1).

in the low energy electrodynamics, including the phonon and interband transition spectra of $Ca_3(Ru_{0.99}Ti_{0.01})_2O_7$. We argue that the optically driven cooperative phenomena result from collective redistribution of electrons within the Ru4d orbital manifolds, which governs the structural distortions of RuO_6 octahedra and spin structures of Ru moments.

2.2. Lattice Distortions Across the Insulator-to-Metal Transition

The disproportionate changes in the crystal lattice parameters across the isostructural IMT ($T_{IMT} = 55$ K) are accompanied by consistent distortions of the RuO_6 octahedra, as illustrated in

Figure 2a–d. These distortions include significant variations in the equatorial Ru–$O_{3,4}$ and apical Ru-$O_{1,2}$ distances (Figure 2a,b), alongside octahedral tilts and rotations (Figure 2c,d), indicating a strong electron-lattice coupling. In the transition, the c-axis compression and octahedral distortions are much stronger than in the parent $Ca_3Ru_2O_7$ compound. One could suggest that the observed photoinduced phase switching is driven by the structural transition, reflected in the behaviour of phonon modes. Excitation of such modes could thus be able to result in the observed switching. To verify this suggestion, we studied the phonon spectra of $Ca_3(Ru_{0.99}Ti_{0.01})_2O_7$ and the impact of phonon pumping on the phase dynamics within the hysteretic region of the IMT.

ADVANCED
SCIENCE NEWS

www.advancedsciencenews.com

ADVANCED
FUNCTIONAL
MATERIALS

www.afm-journal.de

Figure 2. Crystal instability and infrared phonons. a–d) An illustration of the octahedral distortions across the isostructural IMT (T_{IMT} = 55 K). The distortions include changes in the average equatorial $\langle Ru–O_{3,4}\rangle$ and apical $\langle Ru–O_{1,2}\rangle$ distances (a,b) along with rotations of the RuO_6 octahedra expressed in azimuthal φ and polar θ angles for the octahedron diagonal connecting the apical O_1 and O_2 oxygens (c,d). φ and θ correspond to the X_2^+ octahedral rotation and X_3^- octahedral tilt, respectively. e–g) Changes in the phonon spectra along the a-, b-, and c crystallographic axes above and below the IMT. The electronic background present above the transition disappears below T_{IMT}, exposing a number of infrared active phonons. The vertical dotted lines in (e–g) serve as guides to mark the eigenfrequencies of the most pronounced a-axis phonon modes. Arrows indicate the softening of the in-plane stretching modes (e,f) and the hardening of the out-of-plane vibrational mode (g) consistent with the compression of the RuO_6 octahedra along the c-axis, as illustrated in panels (a) and (b). The rise of the mode marked by the asterisk in panel (g) is possibly related to the concomitant rotation and tilting of the RuO_6 octahedra, as illustrated in panels (c) and (d). h) Representative image of the metallic domain structure formed on the surface of the sample, stabilized within the hysteretic region, after irradiation with a fluence of ~100 mJ cm^{-2} at $\hbar\omega \approx$ 70 meV. Similar triangle-shaped metallic flakes, which exhibit thermal decoupling from the bulk material, are observed at different photon energies selected in the shadow range, as depicted in Figure 2e,f. Increased terahertz intensity causes local spots to detach from the sample surface. In screenshot (i), a dark metallic flake (highlighted by a dashed red circle) is seen leaping from the sample.

The concomitant changes of the electronic transport and crystal structure properties across T_{IMT} are captured by the evolution of the infrared phonon spectra, as illustrated in Figure 2e–g. While the electronic background in the metallic state obscures most in-plane phonons, this background is rapidly suppressed below T_{IMT}, revealing the presence of a number of infrared active modes in the insulating phase. From factor group analysis, there are 19 A_1, 19 B_1, and 17 B_2 zone-center infrared active phonon modes that should be observable in the a-, b-, and c-axis spectra, respectively, within the space group $Bb2_1m$.[25] We have identified most of these phonon modes and list their frequencies, linewidths, and oscillator strengths in Table S2 (Supporting Information).[24] The most intense and highest frequency mode, corresponding to Ru–O bond stretching, exhibits a shift in frequency in accordance with the change in the bond distances (Figure 2a,b) that occurs as a result of the c-axis RuO_6 octahedral compression.

As in pristine bilayer $Ca_3Ru_2O_7$, the metallic state above T_{IMT} is quasi-two-dimensional with strong uniaxial anisotropy in the electronic transport.[26,27] The low background in the c-axis IR optical conductivity allows well-defined phonons to be retained across the transition. In addition to the marked shift of phonon frequencies due to changes in the Ru–O bond distances, changes in octahedral orientation (Figure 2c, d) also lead to specific varia-

tions in the phonon spectrum. The increase of these orthorhombic distortions gives rise to phonon features that are not active in the aristotype tetragonal $I4/mmm$ structure. In particular, some of the phonon eigenvectors overlap with a single symmetry-adapted mode of the irreducible representation of $I4/mmm$, which represents either the X_2^+ rotation of the RuO_6 octahedra around the c-axis or the X_3^- diagonal tilting mode.[25] This behavior is demonstrated by the rise of the phonon mode marked by the asterisk at 57 meV in Figure 2g. The observed high sensitivity of the mode intensity is expected for excitations that transform primarily as the X_2^+ and X_3^- irreducible representations, which drive the transition to the polar $Bb2_1m$ phase.[28]

To achieve resonant excitation of the phonon modes in $Ca_3(Ru_{0.99}Ti_{0.01})_2O_7$, we utilized pulses from the Free Electron Lasers for Infrared (IR) eXperiments (FELIX) in Nijmegen, the Netherlands. We used the IR beam with photon energy ranging between 41 and 124 meV, focusing particularly on the vicinity of resonant excitation of the stretching phonon mode, as highlighted in Figure 2e,f by the shadow area. Despite adjusting the photon energy, duration, and repetition rate of the pulses, we were unable to induce the insulator-to-metal phase switching with propagation of the phase interfaces across the full extent of a macroscopic sample, as illustrated in Figure 1d. Instead, the elastic strain created by the IR-excitation results in the formation of
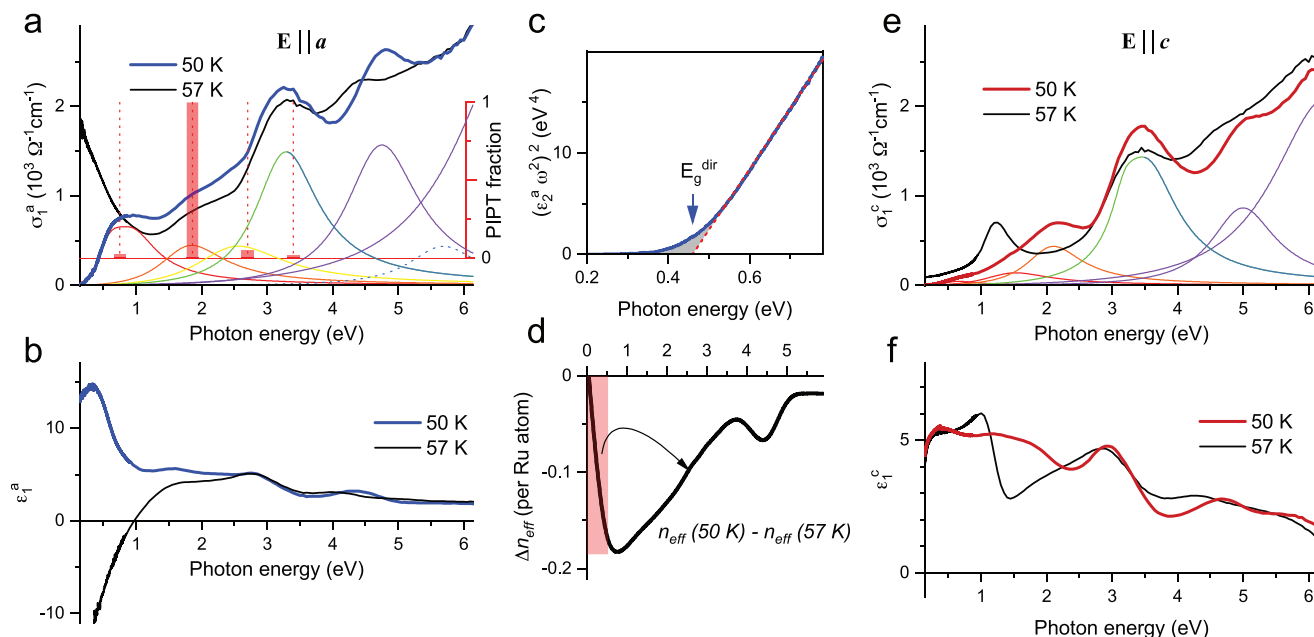
Figure 3. Optical gap and spectral weight transfer across the insulator-to-metal transition. a,b) Real part of the in-plane optical conductivity (a) and dielectric permittivity (b) measured above (thick black) and below (thick blue) T_{IMT}. c) Tauc plot evaluated using the a-axis dielectric function. The linear fit (red dotted line) gives the direct band gap $E_g^{dir} \approx 0.45$ eV. The small sub-gap absorption (gray shaded area) corresponds to minor contribution from Urbach tail states. d) Redistribution of spectral weight upon cooling obtained from integrating the difference of the spectra in (a) in terms of the effective number of electrons per Ru atom, n_{eff}. The in-gap spectral weight (red shaded area) transfers over large energy scales ~5 eV above the gap, pointing to strong electronic correlation effects. e,f) Real part of the optical conductivity and dielectric permittivity measured along the c-axis above (thick black) and below (thick red) T_{IMT}. The thin colored lines in (a) and (e) correspond to separate interband transitions determined by dispersion analysis of the low temperature spectra. The red bars in (a) indicate the volume fraction of the PIPT under constant low irradiance of 20 μW cm^{-2} of monochromatic light at the selected photon energies.
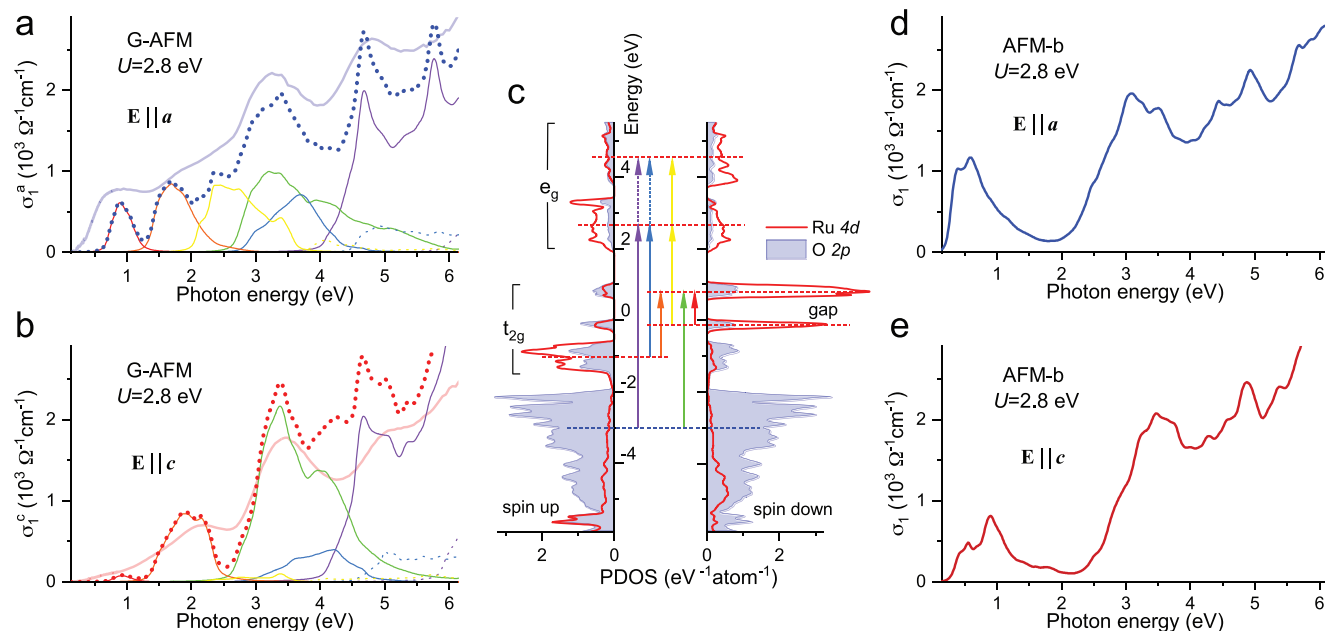
triangle-shaped metallic flakes on the surface (Figure 2h). These flakes are thermally decoupled from the bulk. Further increasing the IR pulse intensity leads to the complete detachment of the flake from the sample surface, as shown in Figure 2i. These irreversible surface changes appear to result from non-adaptive strain generated by the excitation and completely differ from the light-induced effects illustrated in Figure 1d and the recorded Video S3 in the Supporting Information. In search of the trigger for the bulk phase switching, we move to the analysis of interband electronic excitations coupled with the order.

2.3. Mott gap Excitations and Competing Orders

The extent of the opening of the optical gap and associated transfer of spectral weight upon cooling is shown by the broadband (far-IR to UV) optical conductivity $\sigma(\omega)$ and dielectric permittivity $\varepsilon(\omega) = \varepsilon_1(\omega) + i\varepsilon_2(\omega) = 1 + 4\pi i\sigma(\omega)/\omega$ presented in **Figure 3**. In this spectral range the response along the a and b axes does not exhibit appreciable in-plane anisotropy. Above T_{IMT} the PM-M state shows a clear in-plane free-charge-carrier response with negative $\varepsilon_1(\omega)$ below 1 eV, consistent with the corresponding permittivity value in Figure 1b. The metallic response gives an effective carrier density per Ru atom of $n_{eff}^D = 2m/\pi e^2 N_{Ru} \times \omega_p^2/8 \approx 0.4$ e^-/Ru, where m is the free electron mass, $\omega_p \approx 2.8$ eV is the bare plasma frequency, and $N_{Ru} = 1.38 \times 10^{22}$ cm^{-3} is the Ru atom density. Below T_{IMT} a clean optical gap of $E_g^{dir} = 0.45$ eV

opens with a narrow Urbach tail and the in-gap spectral weight, $SW(\Omega) = \int_0^\Omega \sigma_1(\omega)d\omega$, shifts to energies as high as 5-6 eV. This in-gap spectral weight, $n_{eff} = 2m/\pi e^2 N_{Ru} \times SW(E_g^{dir}) \approx 0.2$ e^-/Ru, accounts for as much as half of n_{eff}^D (see Figure 3d). The out-of-plane response in Figure 3e,f, on the other hand, does not display free-charge-carrier behavior, but rather a broad peak centered near 1.2 eV gives rise to the low background in $\sigma_1(\omega)$ at phonon frequencies above T_{IMT} in Figure 2g, suggestive of incoherent interlayer hopping in quasi-two-dimensional Ca$_3$(Ru$_{0.99}$Ti$_{0.01}$)$_2$O$_7$. Upon cooling through T_{IMT}, σ_1^c undergoes significant changes in a similar way as σ_1^a, including the opening of the gap and spectral weight shift to higher energies across the entire spectral range.

We note that even though 1% Ti substitution critically changes the properties of the ground state of the system, this has almost no effect on the optical conductivity spectra of the metallic phase. The electronic structure of pristine Ca$_3$Ru$_2$O$_7$, including its manifestations in optical properties, can be captured well by density functional theory (DFT) band structure calculations[11,29] (for optical conductivity calculations see Supporting Information Figure S6).[24] The severe changes in the spectra across the metal to Mott insulator transition can also be addressed in a straightforward way by taking into account the on-site Coulomb repulsion U within the Ru d shell, which competes with the kinetic energy on the order of the Ru t_{2g} bandwidth W, and results in Hubbard-like band splitting. In order to explain the observed anomalies and the anisotropy of the optical response, spectra obtained from
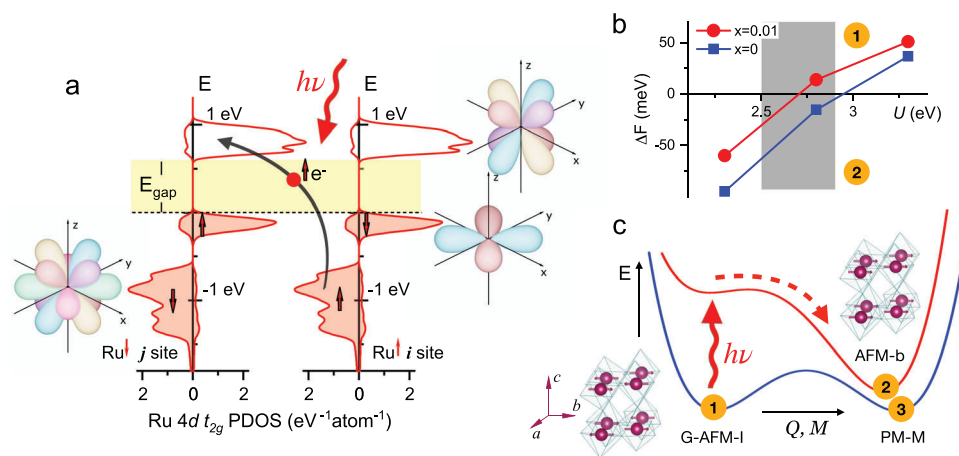
**ADVANCED
SCIENCE NEWS**

www.advancedsciencenews.com

**ADVANCED
FUNCTIONAL
MATERIALS**

www.afm-journal.de

Figure 4. Spin-controlled Mott–Hubbard bands. a,b) Real part of the in-plane (a) and out-of-plane (b) optical conductivity calculated by DFT+U assuming G-AFM magnetic order (thick dotted lines) with a breakdown into separate orbital contributions (thin colored lines). The low-temperature orthorhombic crystal structure of $Ca_3(Ru_{0.99}Ti_{0.01})_2O_7$ is used. The on-site Coulomb repulsion $U = 2.8$ eV is chosen to match the positions of the peaks in the corresponding experimental spectra (semitransparent thick lines and Figure 3a,e). c) Partial densities of the majority spin (spin up, left panel) and minority spin (spin down, right panel) Ru 4d (red lines) and oxygen 2p (blue shaded areas) states. Colors of the vertical arrows denote the orbital character of the separate optical bands in (a) and (b) and in Figure 3a,e. d,e) Uniaxial anisotropy of the optical conductivity calculated by DFT+U assuming AFM-b magnetic order. The crystal structure and the on-site Coulomb repulsion U are the same as in (a) and (b). The ferromagnetic alignment of the Ru moments within the bilayers leads to the suppression of transitions between majority and minority spin-polarized Ru 4d t_{2g} bands (orange peaks in (a) and (b) and arrow in (c) with a shift of the associated spectral weight to the lower energy minority band transitions below 1 eV.

relativistic DFT+U calculations for the experimental crystal structure, assuming G-AFM order, are compared with the measured optical spectra along the a- and c-axes below T_{IMT} (see **Figure 4**a,b, respectively). In contrast to DFT results, the DFT+U solution is insulating, as evidenced by the partial densities of states (PDOS) in Figure 4c. A Mott gap separates empty Ru $d_{xz\downarrow, yz\downarrow}$ from occupied $d_{xy\downarrow}$ states. This orbital ordering within Ru $t_{2g\downarrow}$ states is stabilized due to the compression of RuO$_6$ octahedra below T_{IMT}. With the exchange parameter $J_H = 0.8$ eV, $U = 2.8$ eV is selected by matching the calculated absorption peaks to the experimental spectra, which are decomposed into individual bands in Figure 3a,e by a simultaneous fit of a sum of Lorentzians to $\sigma_1(\omega)$ and $\varepsilon_1(\omega)$ (see Table S3, Supporting Information).[24] The direct bandgap is found to be ∼0.6 eV, fairly consistent with the experimental value. The experimental $E_g^{dir} = 0.45$ eV can be reproduced by decreasing U to 2.5 eV, which still adequately describes the optical transitions.

To identify the optical transition responsible for the PIPT, we illuminate the sample with monochromatic light at selected photon energies near the peak positions in Figure 3a. Only the optical band peaked at 1.85 eV exhibits resonance behavior, where the PIPT is triggered under constant irradiation with average laser intensity as low as 20 μW cm^{-2} following the same dynamics shown in Figure 1d and the Supporting video (Video S3, Figures S4–S6, Supporting Information).[24] What is the specific nature of this resonance? The origin of the absorption

bands in Figure 3a,e is elucidated by comparison with theoretical spectra decomposed into additive contributions calculated as transitions between non-overlapping ranges of initial and final bands (see Figure 4a,b), which are assigned through the analysis of the PDOS in Figure 4c. Two absorption bands, lying at 0.8 eV and 2.5 eV (red and yellow peaks), are assigned to weakly allowed Ru 4d intersite transitions from the occupied $d_{xy\downarrow}$ to the unoccupied $d_{xz\downarrow, yz\downarrow}$ upper Hubbard band and the e_g orbitals, respectively. These transitions are critically sensitive not only to U but also to light polarization and Ru magnetic order within a bilayer, and become almost completely suppressed in the c-axis spectra. On the other hand, the band lying at 1.85 eV (orange peak), consisting of transitions from majority $t_{2g\uparrow}$ to minority $d_{xz\downarrow, yz\downarrow}$, remains largely unchanged between the a- and c-axis spectra. The best overall agreement with the experimental spectra is obtained for G-AFM order, where neighboring Ru ions are aligned antiferromagnetically within the bilayer. Figure 4d,e shows the calculated spectra based on the assumption of an alternative AFM-b magnetic ordering, where Ru ions are aligned ferromagnetically within the bilayer, for comparison. The main absorption peak at 1.85 eV in Figure 4a,b is completely suppressed in Figure 4d,e as $d_{\uparrow} \rightarrow d_{\downarrow}$ transitions between majority and minority spin-polarized Ru 4d t_{2g} bands become forbidden, restricted by the Pauli principle. We assign the PIPT resonance band at 1.85 eV to intersite transitions between neighboring sites i and j of the form $t_{2g}^4(i)t_{2g}^4(j) \rightarrow t_{2g}^3(i)t_{2g}^5(j)$, as

**ADVANCED
SCIENCE NEWS**

www.advancedsciencenews.com

**ADVANCED
FUNCTIONAL
MATERIALS**

www.afm-journal.de

Figure 5. Electronic phase instability and photoinduced phase switching. a) The resonance band at 1.85 eV, attributed to the phase switching behavior, is assigned to intersite transitions between neighboring Ru sites i and j of the form $t_{2g}^{3\uparrow 1\downarrow}(i)$-$t_{2g}^{3\downarrow 1\uparrow}(j) \rightarrow t_{2g}^{2\uparrow 1\downarrow}(i)$-$t_{2g}^{3\downarrow 2\uparrow}(j)$. In the final low-spin $S = 1/2$ local excited state, an electron is transferred (indicated by the black arrow) to the unoccupied minority spin d_{xz} or d_{yz} bands on the neighboring Ru site with an anti-aligned magnetic moment. The orbital character of the occupied (filled red area) and unoccupied (empty red area) Ru $4d\,t_{2g}$ bands is depicted. b) Energy gain between the G-AFM (1) and AFM-b (2) states per formula unit as a function of U for two experimental crystal structures of $Ca_3(Ru_{1-x}Ti_x)_2O_7$, $x = 0$ (blue) and $x = 0.01$ (red). The range of values of U consistent with data in Figure 4 (gray area) corresponds to the degeneracy of the magnetically ordered G-AFM and AFM-b states. c) Conceptual representation of the photoinduced switching between G-AFM-I (1) and PM-M (3) phases with the emergence of the AFM-b (2) ordered hidden state during the process of incoherent relaxation from the photoexcited state. The images of Ru moments (red) surrounded by oxygen octahedra illustrate the magnetically ordered states. The horizontal axis corresponds to the coupled order parameters Q and M, described in the text.

detailed in **Figure 5a**. In the final low-spin $S = 1/2$ local excited state, the electron is transferred to the unoccupied d_{xz} or d_{yz} orbital on the neighboring Ru site with anti-aligned magnetic moment.

Our first-principles DFT+U calculations, based on experimental $Ca_3(Ru_{0.99}Ti_{0.01})_2O_7$ structural parameters and stoichiometric Ca_2RuO_4 composition, provide a comprehensive description of the light-polarization-dependent and spin-controlled low-energy electrodynamics of $Ca_3(Ru_{0.99}Ti_{0.01})_2O_7$ by incorporating the value of U ranging from 2.5 to 2.8 eV. Moreover, the calculations also reveal a critical electronic phase instability with respect to the magnetic order and crystal structure distortions. We calculated the energy difference between G-AFM and AFM-b magnetic orders as a function of U for the crystal structures of pristine $Ca_3Ru_2O_7$ and $Ca_3(Ru_{0.99}Ti_{0.01})_2O_7$ (see Figure 5b). For small U values, a relatively large gain in kinetic energy favors the AFM-b ground state with FM order within bilayers, while stronger electronic correlations stabilize the G-AFM phase. Critically, in the range of values of U defined above (gray shaded area in Figure 5b) these two states are nearly degenerate. By comparing these results (red circles) to the same calculations for the crystal structure parameters of the parent compound (blue squares), we find that the structural distortions addressed in Figure 2a–d also play in favor of the insulating ground state with AFM-ordered nearest-neighbor Ru moments. The relative stability of the G-AFM ground state is achieved by tuning the system through a Mott transition by only 1% replacement of Ru by Ti, which reduces the effective Ru electronic bandwidth W while retaining proximity to the collective instabilities with a high degree of susceptibility to external stimuli. A metastable AFM-b (or AFM-a) phase may manifest itself within the thermal hysteresis due to transient trapping upon fast cooling (see Figure 1c). More sig-

nificantly, the considered intrinsic instabilities in the electronic, magnetic, and structural properties of $Ca_3(Ru_{0.99}Ti_{0.01})_2O_7$ give rise to phase switching triggered by the $d_\uparrow \rightarrow d_\downarrow$ transitions.

2.4. Discussion

The peculiar character of the PIPT excitation band peaked at 1.85 eV, as illustrated in Figure 5b, differs from all other absorption bands in that it involves the specific concomitant change of both the spin state of neighboring Ru atoms ($S = 1 \rightarrow S = 1/2$) and the local orbital polarization ($t_{2g} \rightarrow d_{xz,yz}$), intertwining the charge, spin, and orbital degrees of freedom. The upper bound on the critical density of local excited states is determined by the threshold photon flux of 7×10^{13} s^{-1}cm^{-2}. Photoinduced expansion of the metallic phase across the full extent of the sample volume requires an irradiation time of $10 - 30$ s, giving an estimation of the total photon fluence needed to switch the entire sample that is consistent with the planar (not bulk) density of Ru atoms, $N_{Ru}^{(ab)} = 6.6 \times 10^{14}$ cm^{-2}. This low fluence suggests that bulk switching corresponds to at least $10^5 - 10^6$ Ru states changed per quantum of light absorbed. Such avalanche behavior points to the cooperative interaction between Ru sites photoexcited locally at the interface between the two phases, which mediates the pump-induced motion of the interface and macroscopic expansion of the metallic phase domains.[30]

A formally similar PIPT within the hysteretic region has been detected in conjugated polymers substituted with structurally bistable side groups.[31,32] Despite originating from distinct kinds of instabilities, this phenomenon is generally described by the existence of a free-energy barrier between two material phases

**ADVANCED
SCIENCE NEWS**

www.advancedsciencenews.com

**ADVANCED
FUNCTIONAL
MATERIALS**

www.afm-journal.de

characterized by a set of order parameters coupled biquadratically in the free energy expansion.[33] In this context, during resonant photoexcitation of $Ca_3(Ru_{0.99}Ti_{0.01})_2O_7$, the AFM-$b$ phase, which cannot be attained on the energy surface of the ground state under equilibrium conditions, qualifies as a transient hidden state (Figure 5c). To verify the transient nature of this state, it would be beneficial to employ ultrafast pump-probe time-resolved spectroscopy.

The observed dynamics of photoinduced expansion of one phase with respect to another resembles the scenario that was recently addressed by coupled first- and second-order time-dependent Ginzburg–Landau parameters.[34] Applied to the photoinduced IMT in manganites,[7] a strain-coupled Ginzburg–Landau theory has been considered on the basis of coupled order parameters Q and M, denoting the amplitude of a dominating Jahn–Teller MnO_6 octahedral distortion and the ferromagnetic moment, respectively. A similar approach can also underlie the description of the photoinduced phase transition in $Ca_3(Ru_{0.99}Ti_{0.01})_2O_7$, which is caused by the interplay between the structural RuO_6 distortions and competing AFM and FM spin structures of intra-bilayer Ru moments. The noncentrosymmetric polar $Bb2_1m$ structure dictates some specific features of the structural and magnetic order parameters. First, examining the effect of structural distortions on the phase behavior of isostructural improper ferroelectric insulators $Ca_2Ti_3O_7$ and $Ca_2Mn_3O_7$ reveals that the structural order parameter Q in this class of bilayered perovskites is related to the distortion amplitudes for the individual rotation $(Q_{X_2^+})$ and tilt $(Q_{X_3^-})$ modes that primarily drive the transition to the $Bb2_1m$ from the aristotype $I4/mmm$ phase.[28,35] The hybrid order parameter $Q_{X_{23}} = Q_{X_2^+}Q_{X_3^-}$ defines minima in the double-well potential of the total energy landscape around the reference $I4/mmm$ structure. The same octahedral distortions that produce the polar phase also couple to the magnetic ordering. Second, in contrast to manganites, the itinerant FM state in $Ca_3(Ru_{0.99}Ti_{0.01})_2O_7$ cannot be described by a single magnetic order parameter M because two distinct sublattices of ferromagnetically ordered Ru bilayers, $\mathbf{M}_I$ and $\mathbf{M}_{II}$, are antiferromagnetically coupled and modulated along the c-axis. The phenomena of metamagnetic texture in pristine $Ca_3Ru_2O_7$ has been described by the Ginzburg–Landau theory for the specific coupling between the two order parameters $\mathbf{l} = 1/2(\mathbf{M}_I - \mathbf{M}_{II})$ and $\mathbf{f} = 1/2(\mathbf{M}_I + \mathbf{M}_{II})$, corresponding to the antiferromagnetic staggered magnetization and ferromagnetic spin polarization, respectively.[12] We argue that the above specific features are the key ingredients building the resulting shallow energy landscape in $Ca_3(Ru_{0.99}Ti_{0.01})_2O_7$, whose exceptionally small perturbations by light cause switching between G-AFM-I and PM-M phases within the thermal hysteresis loop.

Another distinct difference from the case of manganites is the coherent insulator-metal domain wall propagation throughout the entire crystal volume under the action of light. The minimum required dilute substitution of Ru in $Ca_3(Ru_{0.99}Ti_{0.01})_2O_7$ needed to establish the Mott insulating ground state leaves the crystal quality almost intact. As a result, there is no marked pinning of the domain walls, and the hysteresis loop in Figure 1b remains essentially symmetrical (see e.g. Ref. [36] for comparison). Increasing the substitution level leads to increased disorder with stronger pinning effects and nanoscale fragmentation of the stripe configuration, and the reg-

ular Ginzburg–Landau phenomenological approach becomes no longer sufficient to describe the pump-induced phase interface motion.[34]

More critically, increasing the substitution of Ru ions further reduces the effective Ru electronic bandwidth W so that the kinetic energy no longer competes with the on-site U. The critical temperature T_{IMT} (which is 55 K for $x = 0.01$ and falls between the two critical temperatures of the pristine $Ca_3Ru_2O_7$, $T_N = 56$ K and $T_s = 48$ K)[21,22] becomes larger for higher x, reaching ≈ 95 K at $x = 0.1$,[23] signifying the stabilization of the Mott insulating state. The collective instabilities in the electronic, magnetic, and structural properties of these compounds and their manifestations in the charge dynamics as discussed above thereby become insensitive to manipulation by light.

3. Conclusion

We have reported here a unique Mott insulator state in $Ca_3(Ru_{0.99}Ti_{0.01})_2O_7$, achieved through delicate control of the one-electron bandwidth W by dilute isovalent substitution of Ru. By combining comprehensive optical measurements (terahertz to UV) with spin-polarized DFT and DFT+U calculations we parameterize this state and assign Hubbard bands associated with the observed optical transitions. The corresponding IMT exhibits exceptional sensitivity to external stimuli such that local low-fluence resonant photoexcitation of Ru $t_{2g}d_\uparrow \rightarrow d_\downarrow$ transitions triggers avalanche-like switching of the entire macroscopic sample to the metallic phase. Moreover, dilute substitution maintains the lattice structure and keeps the crystal quality intact, which is distinct for bandwidth- and filling-controlled Mott IMTs in correlated oxides. From a fundamental perspective, the elimination of pinning effects enables coherent photoinduced motion of the insulator-metal interface and makes $Ca_3(Ru_{0.99}Ti_{0.01})_2O_7$ an ideal model system for building and testing a theory of Mott transition dynamics in the presence of cooperative electron-electron and electron-lattice interactions. At the same time, from a technology perspective, the intact crystal quality and low-fluence light sensitivity pave the way to possible new designs for nanodevices that achieve quantum-level photosensitivity.

4. Experimental Section

Sample Preparation and Characterization: High-quality single crystals of $Ca_3(Ru_{0.99}Ti_{0.01})_2O_7$ were grown using an optical floating-zone technique. Energy dispersive X-ray (EDX) analysis and inductively coupled plasma atomic emission spectroscopy (ICP-AES) verified the uniform sample stoichiometry, and $Ca_3(Ru_{0.99}Ti_{0.01})_2O_7$ crystal structure parameters were derived as a function of temperature based on high-resolution neutron diffraction data. The derived lattice parameters in space group $Bb2_1m$ change across the transition at $T_{IMT} = 55$ K from $a = 5.3685$ Å, $b = 5.5979$ Å, and $c = 19.3478$ Å at 50 K to $a = 5.3659$ Å, $b = 5.5295$ Å, and $c = 19.5359$ Å at 60 K. Neutron diffraction experiments confirmed a pure G-type AFM phase below T_{IMT}. Details of crystal growth and characterization, including crystal and magnetic structure determination, are available in ref. [21]. With special care, only single-domain crystals with characteristic dimensions of $2 \times 2 \times 0.2$ mm³ were selected based on initial examination via reflectivity contrast by polarized-light optical microscopy. Measurements of the magnetization on every selected sample were performed using a vibrating sample magnetometer (see Supporting Information Figure S1).[24] The single crystals were oriented using

backscattering Laue X-ray diffraction (XRD) and supplementary high-resolution XRD measurements with a four-circle setup. The XRD results confirm the monodomain nature of our selected samples, which is further evident in the measured phonon spectra in Figure 2e–g. Samples were cleaved prior to optical measurements. Intrinsic properties could only be obtained for cleaved surfaces, as mechanical treatment such as polishing introduced uncontrolled artifacts due to possible surface damage and strain. Polishing also led to a dramatically broadened transition and shifted T_{IMT}, reflecting the sensitivity of electronic phase instabilities discussed in the main text.

Spectroscopic Ellipsometry: Broadband spectroscopic ellipsometry was used to measure the complex dielectric function, $\varepsilon(\omega) = \varepsilon_1(\omega) + i\varepsilon_2(\omega) = 1 + 4\pi i[\sigma_1(\omega) + i\sigma_2(\omega)]/\omega$, over a range of photon energies extending from the far infrared ($\hbar\omega = 0.01$ eV) into the ultraviolet ($\hbar\omega = 6.5$ eV). The *a*- (*b*- or *c*-) axis component of the dielectric tensor ε_a (ε_b or ε_c) corresponds to the measured pseudodielectric function $\varepsilon_{a,b,c} \approx \tilde{\varepsilon}_{a,b,c}$ at angle of incidence ranging from 70° to 80° for sample orientations with the *a* (*b* or *c*) axis in the plane of incidence. The pseudodielectric function $\tilde{\varepsilon}$ is derived by a direct inversion of the ellipsometric parameters Ψ and Δ assuming bulk isotropic behavior of the sample surface. For details of data acquisition and analysis in the case of optically anisotropic crystals, see refs. [37, 38]. In the frequency range 7.5 meV to 1 eV we used home-built ellipsometers in combination with Bruker IFS 66v/S and Vertex 80v Fourier transform infrared spectrometers. The measurements in the far infrared (7.5 to 88 meV) utilized synchrotron edge radiation of the 2.5 GeV electron storage ring at the IR1 beamline of the Karlsruhe Research Accelerator (KARA) at the Karlsruhe Institute of Technology, Germany. The measurements in the range 0.6–6.5 eV were performed with a Woollam variable angle ellipsometer of rotating-analyzer type.

First-Principles Calculations: The relativistic band structure calculations were performed using the linear muffin-tin orbital (LMTO) method as implemented in PY LMTO computer code.[39] PBESol exchange-correlation potential was used.[40] The Coulomb interaction of Ru 4*d* electrons, in the presence of spin-orbit coupling (SOC), was considered using the rotationally invariant DFT+*U* method,[41] assuming the stoichiometric Ca_2RuO_4 composition. The interband contribution to the imaginary part of the dielectric tensor was calculated using the dipole approximation to the matrix elements of the momentum operator.[39] For the calculations, isovalent Ti substitution was considered via the experimental crystal structure refined for $Ca_3(Ru_{0.99}Ti_{0.01})_2O_7$ at 8K, as reported in ref. [21]. Additional details on the calculations are included in the Supporting Information.[24]

Visualization and Control of the Photoinduced Phase Transition: A reflected-light microscopy setup equipped with a He flow optical cryostat and either a tungsten-halogen white light lamp or monochromatic laser sources of selected photon energies were used to excite and record the PIPT in $Ca_3(Ru_{0.99}Ti_{0.01})_2O_7$. The entire sample surface was evenly illuminated, with control over the integral intensity of the incident light. Representative videos and screenshots are available in the Supporting Information.[24] The bulk and resonant character of the phase switching under low fluence irradiation compared with specific heat data allows us to exclude any light-induced heating effects (see Supporting Information[24]). We used an IR laser pulse excitation at FELIX to investigate the phase switching dynamics under phonon pumping. The central wavelength of the IR pump pulses, with duration in the range of 0.5–1 ps (depending on wavelength), was varied in the spectral range of 10–30 μm with their bandwidth experimentally tunable in the range of 0.5–2.0 % (typically < 1 % of the bandwidth used in our experiments).

Supporting Information

Supporting Information is available from the Wiley Online Library or from the author.

Acknowledgements

Conflict of Interest

The authors declare no conflict of interest.

Data Availability Statement

The data that support the findings of this study are available from the corresponding author upon reasonable request.

Keywords

[1] C. Bao, P. Tang, D. Sun, S. Zhou, *Nat. Rev. Phys.* **2021**, 1.

[2] D. Basov, R. Averitt, D. Hsieh, *Nat. Mater.* **2017**, *16*, 1077.

[3] M. Fiebig, K. Miyano, Y. Tomioka, Y. Tokura, *Science* **1998**, *280*, 1925.

[4] J. Zhang, X. Tan, M. Liu, S. W. Teitelbaum, K. W. Post, F. Jin, K. A. Nelson, D. N. Basov, W. Wu, R. D. Averitt, *Nat. Mater.* **2016**, *15*, 956.

[5] A. de la Torre, D. M. Kennes, M. Claassen, S. Gerber, J. W. McIver, M. A. Sentef, *Rev. Mod. Phys.* **2021**, *93*, 041002.

[6] J. Zhang, R. Averitt, *Annu. Rev. Mater. Res.* **2014**, *44*, 19.

[7] A. S. McLeod, J. Zhang, M. Gu, F. Jin, G. Zhang, K. W. Post, X. Zhao, A. J. Millis, W. Wu, J. M. Rondinelli, R. D. Averitt, D. N. Basov, *Nat. Mater.* **2020**, *19*, 397.

[8] N. Takubo, Y. Ogimoto, M. Nakamura, H. Tamaru, M. Izumi, K. Miyano, *Phys. Rev. Lett.* **2005**, *95*, 017404.

[9] G. Cao, S. McCall, J. E. Crow, R. P. Guertin, *Phys. Rev. Lett.* **1997**, *78*, 1751.

[10] J. S. Lee, S. J. Moon, B. J. Yang, J. Yu, U. Schade, Y. Yoshida, S.-I. Ikeda, T. W. Noh, *Phys. Rev. Lett.* **2007**, *98*, 097403.

[11] I. Marković, M. D. Watson, O. J. Clark, F. Mazzola, E. A. Morales, C. A. Hooley, H. Rosner, C. M. Polley, T. Balasubramanian, S. Mukherjee, N. Kikugawa, D. A. Sokolov, A. P. Mackenzie, P. D. C. King, *Proc. Natl. Acad. Sci. USA* **2020**, *117*, 15524.

[12] D. Sokolov, N. Kikugawa, T. Helm, H. Borrmann, U. Burkhardt, R. Cubitt, J. White, E. Ressouche, M. Bleuel, K. Kummer, A. Mackenzie, U. Rössler, *Nat. Phys.* **2019**, *15*, 671.

[13] S. Lei, M. Gu, D. Puggioni, G. Stone, J. Peng, J. Ge, Y. Wang, B. Wang, Y. Yuan, K. Wang, Z. Mao, J. M. Rondinelli, V. Gopalan, *Nano Lett.* **2018**, *18*, 3088.

[14] M. Horio, Q. Wang, V. Granata, K. P. Kramer, Y. Sassa, S. Jöhr, D. Sutter, A. Bold, L. Das, Y. Xu, R. Frison, R. Fittipaldi, T. K. Kim, C. Cacho, J. E. Rault, P. L. Fèvre, F. Bertran, N. C. Plumb, M. Shi, A. Vecchione, M. H. Fischer, J. Chang, *npj Quantum Mater.* **2021**, *6*, 29.

[15] J. Bertinshaw, M. Krautloher, H. Suzuki, H. Takahashi, A. Ivanov, H. Yavaş, B. J. Kim, H. Gretarsson, B. Keimer, *Phys. Rev. B* **2021**, *103*, 085108.

[16] A. Jain, M. Krautloher, J. Porras, G. Ryu, D. Chen, D. Abernathy, J. Park, A. Ivanov, J. Chaloupka, G. Khaliullin, B. Keimer, B. J. Kim, *Nat. Phys.* **2017**, *13*, 633.

[17] D. Sutter, C. Fatuzzo, S. Moser, M. Kim, R. Fittipaldi, A. Vecchione, V. Granata, Y. Sassa, F. Cossalter, G. Gatti, M. Grioni, H. M. Rønnow, N. C. Plumb, C. E. Matt, M. Shi, M. Hoesch, T. K. Kim, T. R. Chang, H. T. Jeng, C. Jozwiak, *Nat. Commun.* **2017**, *8*, 1.

[18] H. Gretarsson, H. Suzuki, H. Kim, K. Ueda, M. Krautloher, B. J. Kim, H. Yavaş, G. Khaliullin, B. Keimer, *Phys. Rev. B* **2019**, *100*, 045123.

[19] X. Ke, J. Peng, D. J. Singh, T. Hong, W. Tian, C. R. Dela Cruz, Z. Q. Mao, *Phys. Rev. B* **2011**, *84*, 201102.

[20] S. Tsuda, N. Kikugawa, K. Sugii, S. Uji, S. Ueda, M. Nishio, Y. Maeno, *Phys. Rev. B* **2013**, *87*, 241107.

[21] M. Krautloher, Ph.D. Thesis, University of Stuttgart, **2018**, https://elib.uni-stuttgart.de/handle/11682/10315.

[22] W. Bao, Z. Q. Mao, Z. Qu, J. W. Lynn, *Phys. Rev. Lett.* **2008**, *100*, 247203.

[23] A. S. McLeod, A. Wieteska, G. Chiriaco, B. Foutty, Y. Wang, Y. Yuan, F. Xue, V. Gopalan, L. Q. Chen, Z. Q. Mao, A. J. Millis, A. N. Pasupathy, D. N. Basov, *npj Quantum Mater.* **2021**, *6*, 46.

[24] See Supporting Information available from the Wiley Online Library or from the author for more information about experimantal and data analysis.

[25] K. A. Smith, E. A. Nowadnick, S. Fan, O. Khatib, S. J. Lim, B. Gao, N. C. Harms, S. N. Neal, J. K. Kirkland, M. C. Martin, C. J. Won, M. B. Raschke, S.-W. Cheong, C. J. Fennie, G. L. Carr, H. A. Bechtel, J. L. Musfeldt, *Nat. Commun.* **2019**, *10*, 5235.

[26] Y. Yoshida, I. Nagai, S.-I. Ikeda, N. Shirakawa, M. Kosaka, N. Môri, *Phys. Rev. B* **2004**, *69*, 220411.

[27] X. N. Lin, Z. X. Zhou, V. Durairaj, P. Schlottmann, G. Cao, *Phys. Rev. Lett.* **2005**, *95*, 017203.

[28] N. A. Benedek, C. J. Fennie, *Phys. Rev. Lett.* **2011**, *106*, 107204.

[29] D. J. Singh, S. Auluck, *Phys. Rev. Lett.* **2006**, *96*, 097203.

[30] S. Koshihara, T. Ishikawa, Y. Okimoto, K. Onda, R. Fukaya, M. Hada, Y. Hayashi, S. Ishihara, T. Luty, *Phys. Rep.* **2022**, *942*, 1.

[31] S. Koshihara, Y. Tokura, K. Takeda, T. Koda, *Phys. Rev. Lett.* **1992**, *68*, 1148.

[32] N. Hosaka, H. Tachibana, N. Shiga, M. Matsumoto, Y. Tokura, *Phys. Rev. Lett.* **1999**, *82*, 1672.

[33] Y. Tokura, *J. Phys. Soc. Jpn.* **2006**, *75*, 011001.

[34] Z. Sun, A. J. Millis, *Phys. Rev. B* **2020**, *101*, 224305.

[35] M. S. Senn, A. Bombardi, C. A. Murray, C. Vecchini, A. Scherillo, X. Luo, S. W. Cheong, *Phys. Rev. Lett.* **2015**, *114*, 035701.

[36] W. Fan, J. Cao, J. Seidel, Y. Gu, J. W. Yim, C. Barrett, K. M. Yu, J. Ji, R. Ramesh, L. Q. Chen, J. Wu, *Phys. Rev. B* **2011**, *83*, 235102.

[37] T. I. Larkin, A. N. Yaresko, D. Pröpper, K. A. Kikoin, Y. F. Lu, T. Takayama, Y.-L. Mathis, A. W. Rost, H. Takagi, B. Keimer, A. V. Boris, *Phys. Rev. B* **2017**, *95*, 195144.

[38] T. I. Larkin, R. D. Dawson, M. Höppner, T. Takayama, M. Isobe, Y.-L. Mathis, H. Takagi, B. Keimer, A. V. Boris, *Phys. Rev. B* **2018**, *98*, 125113.

[39] V. Antonov, B. Harmon, A. Yaresko, *Electronic structure and magneto-optical properties of solids*, Springer Science & Business Media, **2004**.

[40] J. P. Perdew, A. Ruzsinszky, G. I. Csonka, O. A. Vydrov, G. E. Scuseria, L. A. Constantin, X. Zhou, K. Burke, *Phys. Rev. Lett.* **2008**, *100*, 136406.

[41] A. N. Yaresko, V. N. Antonov, P. Fulde, *Phys. Rev. B* **2003**, *67*, 155103.